

# Visual analysis for microscopic cracking propagation of rubberized concrete



Shuxian Hong<sup>a</sup>, Chuan Kuang<sup>a</sup>, Jianchao Zhang<sup>a,b</sup>, Dongshuai Hou<sup>c</sup>, Jinrui Zhang<sup>d</sup>, Laibao Liu<sup>e</sup>,  
Biqin Dong<sup>a,\*</sup>

<sup>a</sup> School of Civil Engineering, Guangdong Province Key Laboratory of Durability for Marine Civil Engineering, The Key Laboratory on Durability of Civil Engineering in Shenzhen, Shenzhen University, Shenzhen 518060, PR China

<sup>b</sup> Key Laboratory of Earthquake Engineering and Engineering Vibration, Institute of Engineering Mechanics, China Earthquake Administration, Harbin 150080, PR China

<sup>c</sup> Qingdao Technological University, Qingdao 266000, PR China

<sup>d</sup> State Key Laboratory of Hydraulic Engineering Simulation and Safety, Tianjin University, Tianjin 300072, China

<sup>e</sup> State Key Laboratory of Environmental Friendly Energy Materials, Engineering Research Center of Biomass Materials, Ministry of Education, School of Materials Science and Engineering, Southwest University of Science and Technology, Sichuan 621010, China

## HIGHLIGHTS

- A new image processing method is proposed for identifying micro-cracks in concrete using XCT.
- The effect of uneven intensities in the XCT images was overcome.
- Interference of rubber particles and pores on the results of crack detection was avoided.

## ARTICLE INFO

### Article history:

Received 19 February 2020

Received in revised form 27 July 2020

Accepted 13 August 2020

### Keywords:

Rubberized concrete

Cracks propagation

X-ray microcomputed tomography

Microcracks

Image processing

## ABSTRACT

As a combination of a brittle cement matrix and ductile rubber particles, rubberized concrete has complex fracture characteristics at the microscale level. To better understand the fracture pattern of rubberized concrete, in this study, a novel image processing method is developed to extract the cracks in the specimens accurately, especially the microcracks, obtained in X-ray computed tomography images. To demonstrate the validity of the method, in-situ XCT tests were used to track the rubberized concrete specimens under loading. The robustness and practicability of the proposed method were verified by processing the images of the specimens with different rubber contents. The results show that the crack propagation under loading could be visualized by using the method, and the effect of the addition of the rubber on the cracks was then analyzed quantitatively.

© 2020 Elsevier Ltd. All rights reserved.

## 1. Introduction

Rubber consumption has been growing annually worldwide. However, the waste, particularly scrap tires is a significant environmental problem if the rubber is not properly disposed of [1,2]. Thus, considerable attention has been devoted to rubberized concrete due to its high performance and eco-friendly recyclability. Normally, rubberized concrete is made by recycling waste tires and reusing them in concrete [3]. As a new environmental material, rubberized concrete exhibits good cracking shrinkage resistance and impact resistance when compared with the traditional concrete, which is a brittle material [3,4]. Despite the improvements

in the toughness, ductility, impact resistance, dynamic loading behavior, weight, and resistance to cracking due to the addition of rubber into concrete [5,6], the addition of rubber reduces the compressive and tensile strengths of the concrete [7–10]. Many researchers have studied the macroscopic mechanics of rubberized concrete [11–13], but the internal evolution and changes of rubberized concrete during the loading process, particularly the internal cracks, have not been studied significantly [14]. As a combination of a brittle cement matrix and ductile rubber particles, their fracture characteristics are complex at the microscale level [15], which will influence the macro-scale behaviour [16]. Therefore, it is necessary to study the internal cracks of rubberized concrete for its widespread use in structural reinforced concrete elements [17].

\* Corresponding author.

E-mail address: [incise@szu.edu.cn](mailto:incise@szu.edu.cn) (B. Dong).

In recent years, the cracking propagation in cement-based materials has been detected by non-destructive XCT testing, such as cracking propagation in mortar [18], gravel concrete [19], and cement paste [20]. As a combination of concrete and rubber particles, rubberized concrete has a complicated structure based on its microstructural characteristics [15] and contains more microcracks than other kinds of concrete [21,22], particularly mortar. Besides, the intensity for the same material in the images varies in different regions due to beam hardening artifacts [23,24]. Furthermore, cracks propagate through the pores in the images, which makes it hard to differentiate the cracks from the pores. Thus, the images of rubberized concrete from XCT testing are more complex than that of traditional concrete. In previous research, the global threshold methods, such as Otsu's method [25], are widely used by simply using the grey values to distinguish the aggregate, cement, voids, and cracks in the XCT images [26,27]. However, these studies often fail to consider the effects of noise and uneven intensities [28], and pores connected to the cracks are always evident in the final 3D image [19,29,30]. These characteristics mentioned above make it very difficult to identify the cracks using conventional image processing methods based on a single threshold of gray intensity [31]. In addition, the cracks are often detected in two dimensions, in which the information of the third dimension is lost, which introduces errors in the final images. Furthermore, advanced local thresholding methods, such as Sauvola's method [32,33], in which the threshold is computed at each block of pixels of an image [28], can improve the quality of the surface of the CT image and reduce the effect of artifacts [34]. However, these methods failed to separate the pores connected to the cracks and detect the true boundary of the specimen. Therefore, existing methods are not suitable for processing the XCT images of rubber concrete.

To solve the above-mentioned problems, a new image processing procedure is proposed. In this method, the boundary of the specimen is detected, especially the cracks connected to the outside air. Local threshold segmentation was applied to the region to reduce the effect of the uneven intensities, in which more microcracks were found. Moreover, the cracks were extracted by separation, where the pores, including those connected to the cracks, were removed, and the errors were reduced effectively. To demonstrate the effectiveness of the method, the fracture processes of rubberized concrete with three rubber content levels (5%, 10%, and 15%) were investigated using in-situ loading X-ray computed tomography (XCT). Using the method, 3D images of the cracks in the specimens in the loading process were visualized and qualitatively analyzed. In addition, the advantages and the accuracy of the method in the paper over the traditional method are compared.

## 2. Materials and tests

### 2.1. Specimen preparation

The cement used in the study was P.O. 42.5, and sand was obtained by passing the standard sand through 200  $\mu\text{m}$  sieve and an apparent density of 2810  $\text{kg}/\text{m}^3$ . The mixed rubber comprised spherical rubber powder with particles sizes of 125–180  $\mu\text{m}$ , with an apparent density of 720  $\text{kg}/\text{m}^3$ . The weight ratio of sand, cement, and water was 4:2:1. The sand was partially replaced with rubber at contents of 5%, 10%, and 15% by volume. After being mixed and stirred, the fresh mixture was cast into  $10 \times 10 \times 10 \text{ mm}^3$  cube molds and then cured together with the molds in a standard curing room ( $95 \pm 5\% \text{ RH}$ ,  $20 \pm 2 \text{ }^\circ\text{C}$ ) for 24 h. The samples with relatively small dimensions were used to avoid micro-cracks and initial defects introduced when the samples were cut from a larger size, which resulted in an easier occurrence of cracks [35,36]. The samples were then de-molded and cured in

the water until the test age. Before the XCT scan test, the surface of the specimen was polished using sandpaper so that the specimen contact surface could be evenly stressed when loading. There were seven specimens for each group; among them, one was used for the in-situ XCT loading tests, whereas the remaining six were prepared to determine the ultimate load.

### 2.2. Test method

The in-situ XCT (XRadia Micro XCT-400, USA) test was carried out for each specimen at different loading stages. As shown in Table 1, several key parameters were used in the test. The intensity of each voxel in the obtained XCT images was set to values from 0 to 65,535 based on the X-ray absorption coefficient of the material at the corresponding position. A loading platform that could be moved upward was lifted to load the specimens and equipped inside the loading rig. At each stage, the load was increased to the reserved value, and the displacement was kept constant and rotated  $360^\circ$  with the loading rig. A  $360^\circ$  scan was completed before loading it to the next level of loading. The detailed loading method was as follows. The specimens were loaded at a speed of 0.1 mm/min and sampled every 500 ms. The specimen was first scanned without the load. XCT scanning was then performed at loads of 50% and 90% of the ultimate load. The ultimate load was determined by the remaining six groups of specimens with the same rubber content referring to the loading method in the standard GBT 17671-1999 [37]. Finally, the specimen was loaded to destruction (ultimate load), and the last scan was performed. The loads of the four scans on specimens with different rubber contents are shown in Table 2.

## 3. Proposed method for processing image

The raw XCT projection images of the rubberized concrete often contain cement paste, outside air, pores, rubber particles, unhydrated cement, and cracks. To obtain the images of the cracks in a specimen, the method illustrated in Fig. 1 was developed. The input was a 3D raw XCT image, and the output was the 3D image of the cracks in the specimen. The procedure, as shown in Fig. 1, contained the following steps:

- 1) The raw XCT projection images were sliced into multiple 2D sections with different orientations to obtain three sets of images  $f^0(f_x^0, f_y^0, f_z^0)$ .
- 2) The boundary of the specimen in the images  $f^0$  was detected, where the region with the crack connected to the outside air was closed to observe the true edge and obtain the images  $g(g_x, g_y, g_z)$ . Most of the outside air was removed, and the region showing the specimen was retained.
- 3) Local threshold segmentation was applied to images  $g$  to obtain the new binary images  $f_s^1(f_{sx}^1, f_{sy}^1, f_{sz}^1)$  that contained the cracks, residual air (the residual outside air in detecting the boundary), rubber particles, and pores.
- 4) The cracks were distinguished from images  $f_s^1$  using a two-dimensional separation process based on the shape parameters to obtain sectional images  $F$  with three different orientations. To remove the pores, which were connected to some cracks, and the errors, a three-dimensional separation was applied to images  $F$  to obtain a final three-dimensional image of the cracks in the specimen.

In steps 2–3, multiple 2D sections with different orientations  $X, Y, Z$  were processed, respectively. Key points of the procedure are described in detail in the next section.

**Table 1**  
Scanning parameters of the XCT test.

Voltage (kV)	Current ( $\mu$ A)	Magnification ( $\times$ )	Exposure time (s)	Image matrix size (voxel)	Voxel physical size ( $\mu\text{m}^3$ )
80	100	0.4	8	$1024 \times 1024 \times 1000$	$14.2735 \times 14.2735 \times 14.2735$

**Table 2**  
Loads(N) of the four scans on specimens with different rubber contents.

No.	1st scan	2nd scan	3rd scan	4th scan
5%	0	850	1600	1850
10%	0	800	1350	1550
15%	0	650	1250	1400

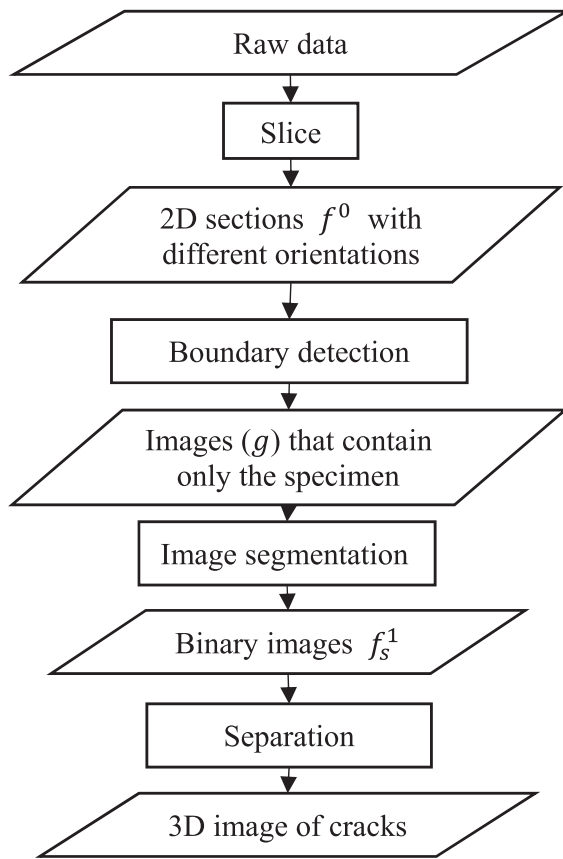


**Fig. 1.** Procedure of the proposed method.

## 5. Boundary detection

Before the boundary detection, the raw data were sliced into multiple 2D sections with different orientations  $X, Y, Z$  to obtain three sets of images  $f^0 (f_x^0, f_y^0, f_z^0)$ , respectively. To obtain the region of the specimen, it was necessary to detect the boundary after closing the region. Because there were always regions where the cracks were connected to the outside air and their voxel values were very close, the cracks were hard to distinguish. Therefore, a transformation function in the proposed method was built to close the regions.

### Step 1. Intensity normalization:

The normalization can eliminate the influence of high-frequency noise and very low noise, providing convenience for

the calculations in the subsequent image processing steps. Therefore, max-min normalization was applied to the image  $f^0$ , and the output image  $f$  was obtained.

### Step 2. Intensity transformation:

Let  $(x, y)$  be the coordinate of a voxel. The origin of an image is defined at the top left corner, and the Cartesian right-hand coordinate system as shown in Fig. 2 is used in the proposed method.

An intensity transformation function in Fig. 2 is applied to the image  $f$  to obtain the image  $s$  to close the cracks connected to the outside air. As shown in Fig. 2, the abscissa axis is the input intensities  $f(x, y)$  in the raw XCT image, the ordinate axis is the output intensities  $s(x, y)$  after the transformation. The maximum intensities of the input and the output image both equal  $L-1$ . Moreover, the specific intensity transformation in Fig. 2 can be obtained in Eqs. (1) and (2) as follows:

$$s(x, y) = \begin{cases} 0 & f(x, y) < pT \\ V[f(x, y)] & pT \leq f(x, y) < T + pT \\ 1 & T + pT \leq f(x, y) \end{cases} \quad (1)$$

where  $f(x, y)$  is the intensity of a voxel at the point  $(x, y)$  in the image  $f$ ,  $s(x, y)$  is the intensity of a voxel at the point  $(x, y)$  in the image  $s$ ,  $p$  is a percentage, and  $T$  is a threshold to distinguish the gas and solid phases.  $s(x, y)$  is a function used to normalize the region except where the voxel value is too high or too low. When the intensity  $f(x, y)$  at the point  $(x, y)$  in the raw XCT image  $f$  is less than  $pT + T$  and not less than  $pT$ , the transformed intensity at the point is calculated by the nonlinear function  $V$  in Eq. (2) as illustrated as follows:

$$V[f(x, y)] = \left( \frac{f(x, y) - pT}{T} \right)^{lam} \quad (2)$$

where  $lam$  is a positive constant ( $0 < lam < 1$ ). When the input image is given, the cracks that are connected with the outside air in the output image  $s$  can be closed by setting the appropriate parameters  $p$  and  $lam$ .  $lam$  and  $p$  are critical in the intensity transformation and will further affect the result of the boundary identification. Besides, a suitable  $lam$  and  $p$  will get a better output image

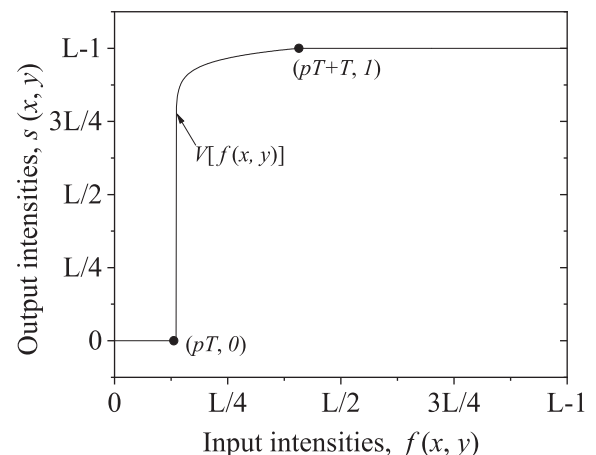


**Fig. 2.** Intensity transformation function. The maximum intensities of the input image  $f$  and the output image  $s$  are both  $L-1$ .

that only contains the sample area after boundary detection. Therefore, we used the current  $lam$  and  $p$  as variables in the actual programming and made the boundary detection on selected typical XCT images. Then, we observed and compared the edge of the sample in the output images under different variables with the true edge of the samples in the original images to get the appropriate  $lam$  and  $p$ .

### Step 3. Boundary identification:

The boundary image  $L$  is obtained by applying edge detection to the output image  $s$ , and then the values of the inside of the boundary in the image  $s$  are set to 1 to obtain the mask of specimen region  $M$ .  $L$  and  $M$  are binary images with backgrounds of 0 and foregrounds of 1.  $g^0$  is an output image in which the region outside the specimen in the original image  $f^0$  is processed as the background by the mask  $M$ :

$$g^0(x, y) = f^0(x, y)M(x, y). \quad (3)$$

However, the minimum intensity of the specimen region was too high, compared with that of the background, to achieve segmentation. To improve the contrast, the intensity of the specimen region was transformed to 0–255 with the max-min normalization to obtain the image  $g$ .

## 6. Image segmentation

After the boundary detection, the voxels of images  $g$  that contain only the specimen would be divided into the background with an intensity 0 and foreground with an intensity 255 according to the threshold, and the image  $f_s(x, y)$  is obtained as a result. Considering that the X-rays are spatially non-uniform in practice due to the beam hardening artifact, it is more reasonable to set the threshold using a local adaptive thresholding method. In this study, Savola's method [32,33] is used to compute the threshold  $H(x, y)$  at the point  $(x, y)$  because this method can prevent the imposition of noise on an object and provide more precise separation of an object from the background noise [28], which is shown as follows:

$$H(x, y) = \left[ k \left( \frac{s_0(x, y)}{R} - 1 \right) + 1 \right] m(x, y), \quad (4)$$

where  $R$  equals 128,  $k$  is the sensitivity in the range (0, 1),  $s_0(x, y)$  and  $m(x, y)$  are a standard deviation and the mean in the neighborhood of the point  $(x, y)$ , and  $s_0(x, y)$  and  $m(x, y)$  are calculated in a window with the size of  $w \times w$ , which is centered on the point  $(x, y)$ . To obtain images of the inside rubber particles, pores, and cracks, the following equation was used:

$$f_s^1(x, y) = 255 \times M(x, y) - f_s(x, y), \quad (5)$$

where  $M$  is the mask of the specimen region, which is a binary image with a background of 0 and a foreground of 1, and the input image is also a binary image  $f_s(x, y)$  with a background of 0 and a foreground of 255. The output  $f_s^1(x, y)$  is the binary image of pores, cracks, rubber particles, and residual edges in the specimen.

### 6.1. Separation

#### 6.1.1. Two-dimensional separation

In the last step of the operation, there were some regions where a crack, such as the region B# in Fig. 6(b), was connected to the remnants of the outside air in the binary image  $f_s^1$  that only contained pores, cracks, rubber particles, and residual edges. It was necessary to break the connection points and the four edge corners of the outside air before labeling the image. After the operation, the remnants could be distinguished from the crack when labeling

them. The proposed method uses a  $5 \times 5$  window to label the connected regions.

As shown in Fig. 3, the 24 neighbors of a voxel  $p$  at coordinates  $(x, y)$  in an image have the next 24 coordinates:

$$x \pm i, y \pm j (i = -2, -1, 1, 2, j = -2, -1, 0, 1, 2), \\ (x, y \pm j) (j = -2, -1, 1, 2).$$

The set of image locations of the neighborhood of the red square point is called  $N_{24}(p)$ . The 24-connected component is defined as follows. In a binary image, two voxels  $p$  and  $q$  with values of 255 are in a 24-connected component if  $q$  is in the set  $N_{24}(p)$ . The 24-connected component labeling can be completed by the two-pass connected-component labeling algorithm [38].

After labeling the image, a two-dimensional separation based on the shape is established to make it possible to determine which object a component in the labeling image belongs to. The parameters used in the separator are defined as follows.

**Slender index:** The extraction parameter  $p^k$  is used to distinguish the slender and round components, which is defined as follows:

$$p^k = \left( d_{max}^k \times d_{min}^k \right) / \left( d_o^k \right)^2, \quad (6)$$

where  $k$  is the sequence number of a 24-connected component in the slice image,  $d_{max}^k$  is the maximum Feret diameter [39] of the foreground in the component image  $g^k(x, y)$ ,  $d_{min}^k$  is the minimum, and the equivalent diameter  $d_o^k$  is computed using Eq. (8) (shown below). The output value  $p$  is called the slender index. When the region is a circle,  $p = 1$ ; when it is a square,  $p = \sqrt{2}\pi/4$ , when it was a regular triangle,  $p = \pi/2$ . The components with a shape similar to the circle, the square, and the regular triangle, of which the slender indexes range from 1 to  $\pi/2$ , are taken as a pore or a rubberized particle and the rest are cracks as shown in Table 3.

**Center coordinates:** The center coordinate of a connected component can be calculated as follows

$$(x_o^k, y_o^k) = \left( \sum_{i=1}^m x_i^k / m, \sum_{i=1}^m y_i^k / m \right), \quad (7)$$

where the number of voxels in the connected region is  $m$ , and coordinates of the voxels in the connected region are marked with a number  $k$ . The coordinate values of the edge residual portion are

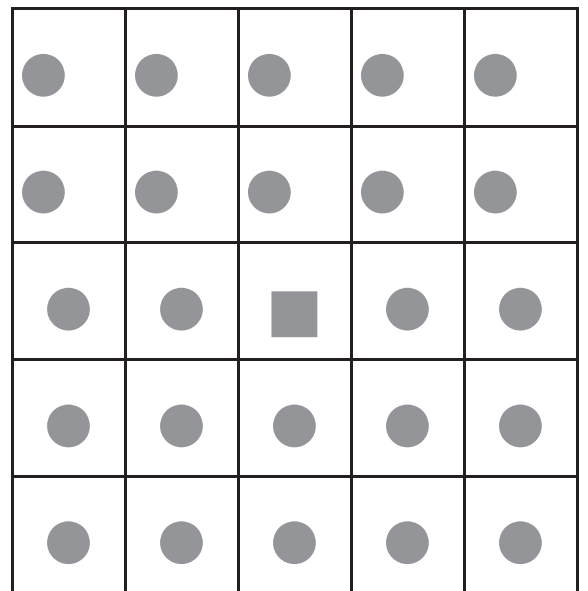


Fig. 3. 24-Connected neighbors.

**Table 3**

Shape conditions used to identify different objects in the specimen.

Name	$p^k$	Centers $(x_0^k, y_0^k)$
Condition (1)		$x_0 \in (x_{min} + t, x_{max} - t) y_0 \in (y_{min} + t, y_{max} - t)$
Condition (2)	$[1, \pi/2]$	

always the largest or smallest, so we can set a threshold to distinguish the edge residual.

*Equivalent diameter:*

When the image is two-dimensional

$$d_o^k = \sqrt{4S^k/\pi}, \quad (8)$$

where the input  $S^k$  is the area of a component  $k$ , and the output  $d_o^k$  is used in Eq. (6).

The shape parameters of different objects in the specimen are shown in Table 3.

As condition (1) shown in Table 3,  $x_{max}, y_{min}, x_{max}, y_{max}$  are the extreme values of the center coordinates in Eq. (7), and  $t$  is a threshold for judging whether the component is close to the edge of the sample to remove the residual air. Moreover, it can be known from the previous discussion that the slender index of pores and rubber particles in the images is in  $[1, \pi/2]$ , so the interval  $[1, \pi/2]$  is determined as condition (2) to distinguish cracks from pores and rubber particles.

According to the parameter characteristics, a two-dimensional separation based on the shape, as shown in Fig. 4, was used to distinguish the residual edges and cracks by the following steps:

- 1) The image  $Q_0$  was duplicated, the holes in each component were filled, and the image  $Q_1$  was obtained.
- 2) The shape parameters of all the components in the images  $Q_0$  and  $Q_1$  were computed, and the parameters  $U_1$  and  $U_2$  were obtained.
- 3) When  $U_1$  did not satisfy condition (1), the corresponding components taken as the residue of the outside air were separated from the image  $Q_0$  to obtain the image of the cracks, pores, and rubber particles  $Q_2$ .
- 4) When  $U_1$  did not meet condition (2), the corresponding components were taken as the cracks, and the sectional image  $F$  of the cracks was obtained.

In the image  $Q_0$ , a component that resembled a circle but contained voids had a slender index  $p^k$  with a large value. To be correctly classified, the voids inside were filled to compute the shape parameters to meet condition (2). To avoid changing the shape of the components of the cracks in the final images, this operation was applied to a copy of the image  $Q_0$ .

After the image segmentation and the two-dimensional separation were successively applied, the sectional images  $F$  of the cracks with different orientations  $X, Y, Z$  were obtained.

### 6.1.2. Three-dimensional separation

When the two-dimensional separation was complete, the cracks were initially separated as the output images  $F$  with different orientations. However, many pores were still connected to the cracks, and the errors in the sectional images were caused by the lack of information on the third dimension when processing the images. To remove the pores and reduce the errors, a three-dimensional separation in the proposed method was applied to these sectional images  $F$ . Thus, three sets of the sectional images (2D matrices) were stacked to form three 3D images (3D matrices, in general), and the intersection of the 3D images was computed as follows:

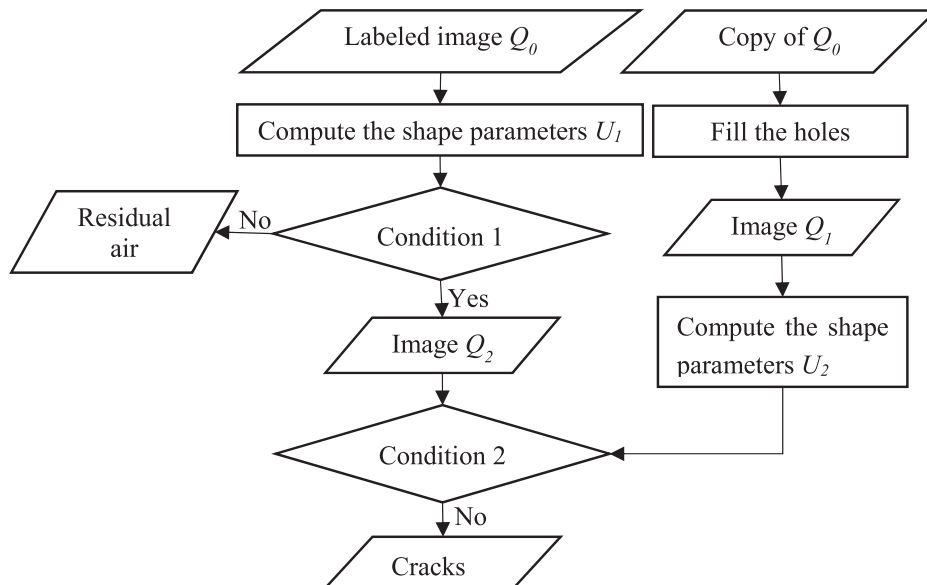
$$F_{3D}(x, y, z) = F_{3D}^X(x, y, z) \times F_{3D}^Y(x, y, z) \times F_{3D}^Z(x, y, z), \quad (9)$$

which represents the multiplication of intensities at the point  $(x, y, z)$  in the three three-dimensional images  $F_{3D}^X, F_{3D}^Y, F_{3D}^Z$ , and the output is the intensity at the same position in the final image  $F_{3D}$ .

## 7. Results and discussion

### 7.1. Image processing

The cracks in the specimen were identified after processing the images obtained from XCT testing following the procedure in Fig. 1. A typical sectional image with the orientation  $Z$  of the raw XCT image is shown in Fig. 5 (a). Traditional methods, such as Otsu's method [25], as shown in Fig. 5(b), failed to detect the crack in area A# in Fig. 5(a), where some parts of the inside crack around the edge were connected with the outside air.

**Fig. 4.** Two-dimensional separation.



To recognize the kind of cracks, the intensity transformation function expressed in Eqs. (1) and (2) was used to close the connected region, as shown in area A# in Fig. 5(c), and the result is shown in Fig. 5(d). As for the function transformation in Eq. (1), the parameter  $T$  was the threshold computed in Otsu's method,  $p$  was set to 0.7, and the intensities of the voxels in the region less than  $(1+p)T$  and more than  $pT$  in Fig. 5(c) were taken as the part non-linear transformation interval in Eq. (1). After the transformation, edge detection was applied to Fig. 5(d), and the image only containing the image region of the specimen was obtained, as shown in Fig. 5(e), in which the outside region was set as the background in Eq. (3). As shown in Fig. 5(f), the true boundary of the specimen could be recognized, as seen in area A#, using the proposed method.

After the boundary detection, the specimen region was retained, and most of the outside air was set as the background, as shown in Fig. 5(e). However, the cracks in Fig. 5(e) have very similar intensities to those of the pores, rubber particles, and residual air, so it is difficult to distinguish them only by segmentation. Therefore, after the image segmentation in Eqs. (4) and (5) were applied to Fig. 5(e) and the image shown in Fig. 6(a) was obtained, the two-dimensional separation in Fig. 4 was then applied to the results of the segmentation, and the obtained image of the cracks is shown in Fig. 6(b). During the segmentation, the window size in Eq. (4) was set to 15 voxels, and  $k$  was set to 0.1.

Before applying the 24-connected component labeling in the two-dimensional separation to Fig. 6(a), some cracks in area B# in Fig. 6(a) were connected to the residual air, which was treated

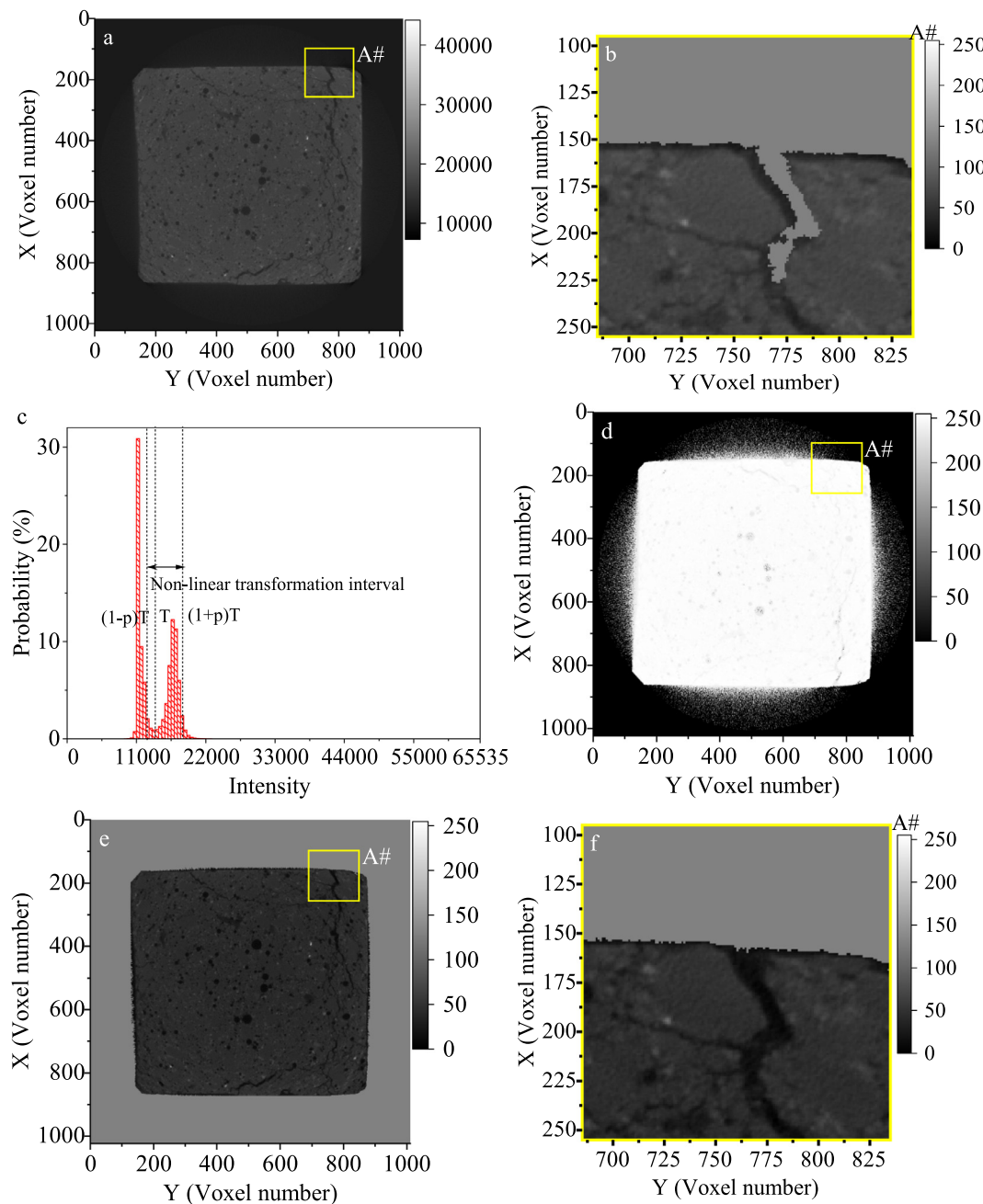


**Fig. 5.** Intensity transformation results: (a) original image; (b) area A# from the detection using Otsu's method; (c) the histogram of the intensities of (a), where  $pT$ ,  $T$ , and  $pT + T$  are the parameters of the non-linear intensity transformation function in Eq. (1); (d) result of the transformation; (e) result of the boundary detection in the proposed method; and (f) area A# in (e). The intensities of the backgrounds in (b), (e), and (f) were changed from 0 to 128 to be better displayed, but the actual values did not change.

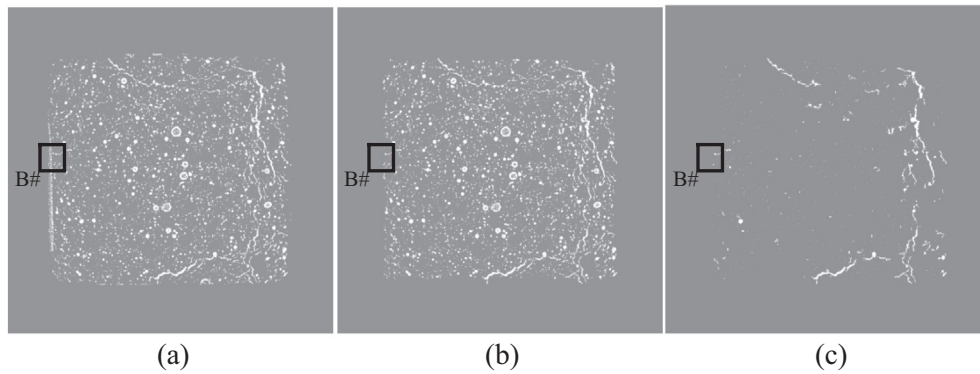


**Fig. 6.** Image segmentation and separation: (a) the result of applying the image segmentation to the image in Fig. 5(a); (b) the image with the residual air removed; (c) the cracks. The values of the backgrounds in all the images (a–c) were changed from 0 to 128 to be better displayed, whereas the actual values were not changed in the actual operation.

as one component. Thus, it was necessary to break the connection to identify the crack in area B# in Fig. 6(c). As shown in Fig. 6(b), the residual air was removed after the points were broken a few times.

The image segmentation and the two-dimensional separation were applied to obtain a set of 2D images of the cracks in the Z orientation, which were reconstructed into the 3D image in Fig. 7(a). As shown in Fig. 7(b, c), the 3D images of the cracks reconstructed from the sectional results in the X and Y orientations were obtained in the same way. The intersection of Fig. 7(a–c) was taken as the final image of the cracks, as shown in Fig. 7(d).

To demonstrate the improvement from the intersection, typical sections in the same position of the images of the cracks are shown

in Fig. 8(a–c), which was, respectively, processed in the Z, Y, and X orientation. As shown in Fig. 8(d), the pores that were connected to the cracks were removed, and the errors caused by the lack of the information of the third dimension when processing the images were also reduced after the three-dimensional separation based on the intersection.

## 7.2. Comparative analysis of different image segmentation methods

The image segmentation in the proposed method is Sauvola's thresholding algorithm, where a local threshold segmentation is applied to the specimen region after the boundary detection. While Sauvola's thresholding algorithm uses a typical local threshold

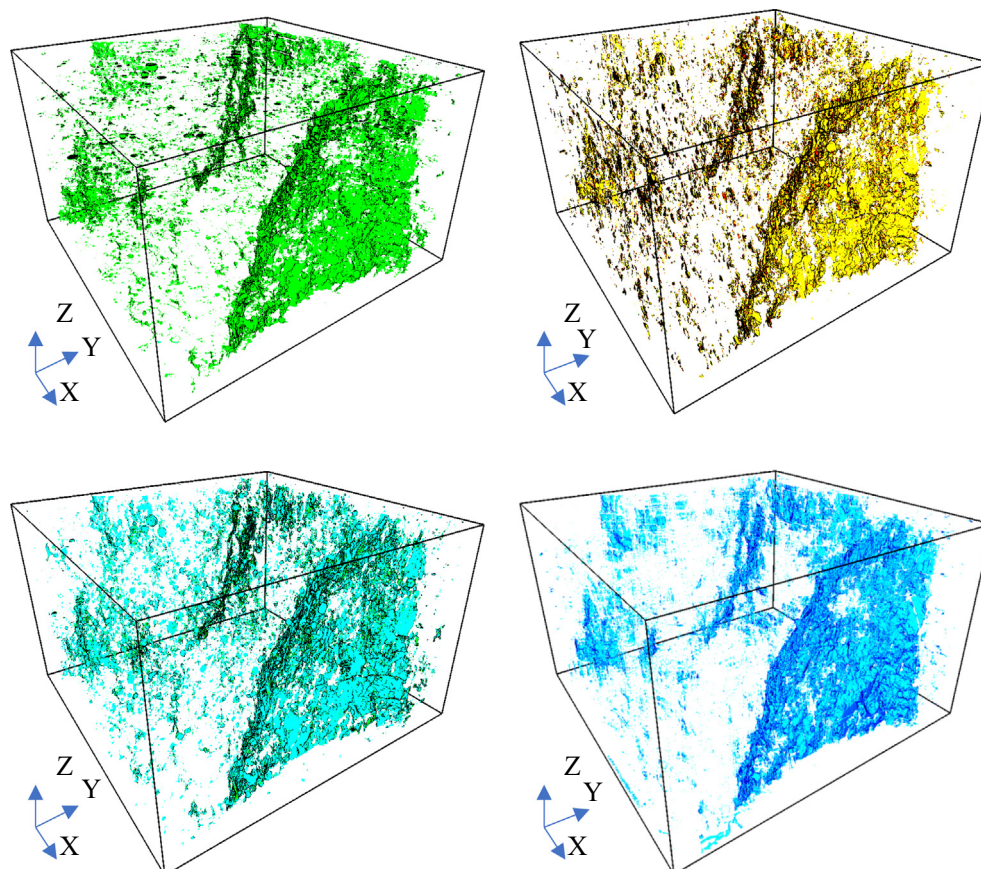


**Fig. 7.** Intersection of the 3D images by the process in different orientations: (a) the 3D image of the cracks in the orientation Y, (b) the 3D image of the cracks in the orientation X, and (c) the final image of the cracks, which was the intersection of the images in (a)–(c).

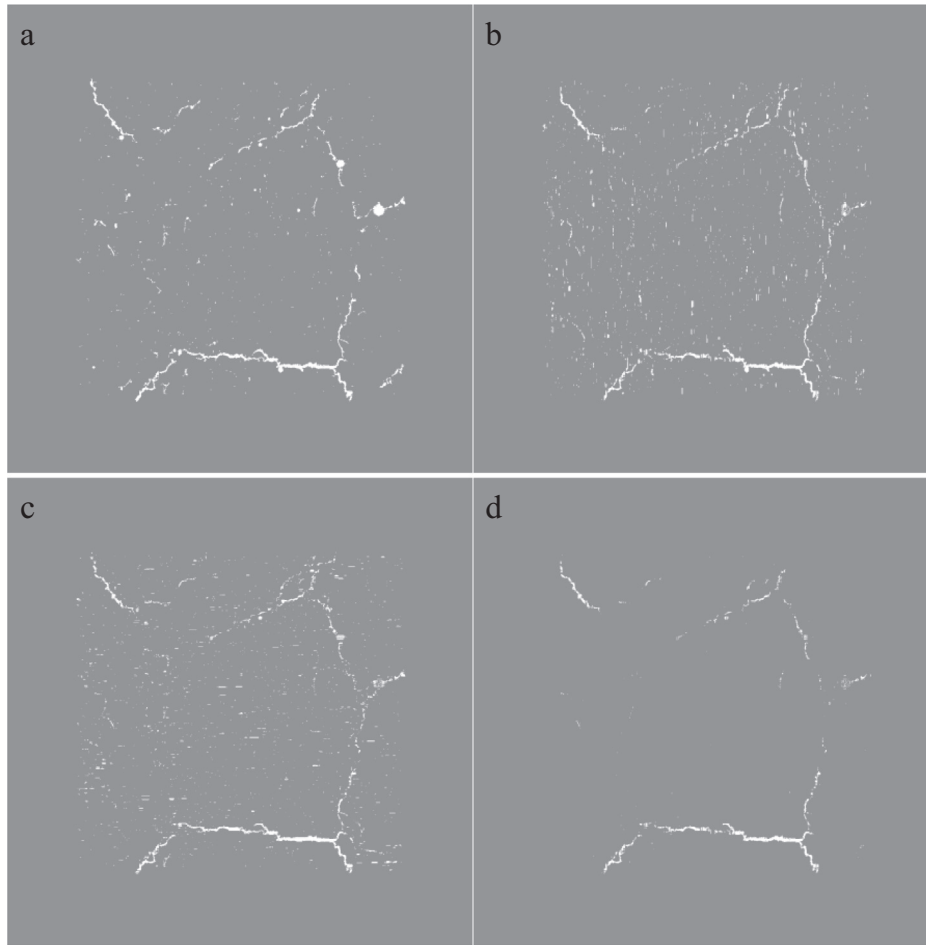


**Fig. 8.** Improvement from the intersection: (a) the section of the 3D image of the cracks only processed in the Z orientation; (b) the section in the same position of the 3D image of the cracks only processed in the Y orientation; (c) the section in the same position of the 3D image of the cracks only processed in the X orientation; (d) the section in the same position of the 3D image of the cracks after the three-dimensional separation based on the intersection. The background values in all the images (a–d) were changed from 0 to 128 to be better displayed, whereas the actual values were not changed in the actual operation.

method, Otsu's method uses a typical global threshold and has been commonly used in concrete image segmentation [40,41]. The three methods were applied to the twenty-fifth image sliced in the loading orientation of the specimen with a 5% rubber content, and a comparison was made based on the results, as shown in Fig. 9. Thresholds for the segmentation at all the voxels on the line  $Y = 630$  (voxel number, the white line in Fig. 9(a)) were computed by Otsu's method, Sauvola's method, and the proposed method to be compared with the actual intensity to decide whether a voxel belonged to a crack.

When the intensity at a voxel was lower than the threshold obtained by one of the three methods, it was taken as a crack. Area C# in Fig. 9(b), where a small crack was present at point P, was not correctly recognized by Otsu's and Sauvola's methods, whereas it was recognized by the proposed method shown in Fig. 9(d, f). Therefore, the proposed method could locate microcracks, whereas traditional methods could not.

As the proposed method is designed to be more sensitive to the change of the intensity with the position, as in Eq. (4), the thresholds in the proposed method were closer to the intensities in the images than those of the other methods, as shown in Fig. 9(c, e). Otsu's method found 21 voxels of the objects from 180 to 850 (voxel number) on the white line, Savola's method found 34, and the proposed method found 170, as determined by the statistical analysis of the data shown in Fig. 9(c, e). Consequently, the proposed method was more effective at detecting the cracks.

To evaluate the accuracy of the detection, the three methods were applied to detect the cracks in Fig. 9(a), and the cracks were obtained from the binary images by the two-dimensional separation. To evaluate the accuracy in terms of the area of the cracks, the actual cracks in the image in Fig. 9(a) were manually marked, as shown in Fig. 10(d). The following index was defined to quantify the results of the area of the cracks:

$$E_{Area}(t) = S_0 \sum_{i=1}^t \sum_{j=1}^{1024} S_{crack}(i, j) (i, t = 1, 2, \dots, 1024) \quad (10)$$

where  $S_{crack}(i, j)$  is 0 by default but equals 1 when a crack is present at the point  $(i, j)$  in an image, and  $S_0$  is a unit area of  $14.2735^2 \mu\text{m}^2$ . The output  $E_{Area}(t)$  is the cumulative area from 1 to  $t$  in the orientation X.

The cumulative area in Fig. 10(a–c) was calculated using Eq. (10), and the results of the three methods are presented in Fig. 10(e). Using the proposed method, the loss of the final cumulative area reduced from more than 90% of the total actual area to 38%. Moreover, the number of cracks in Fig. 10(b–c) detected by Savola's method and that by the proposed method are both significantly higher than that by Otsu's method in Fig. 10(a), which shows that the first two methods could effectively overcome the effect of the uneven intensity when detecting the cracks. Meanwhile, the proposed method found more complete cracks than Savola's method as shown in Fig. 10(b–c), which should be the rea-



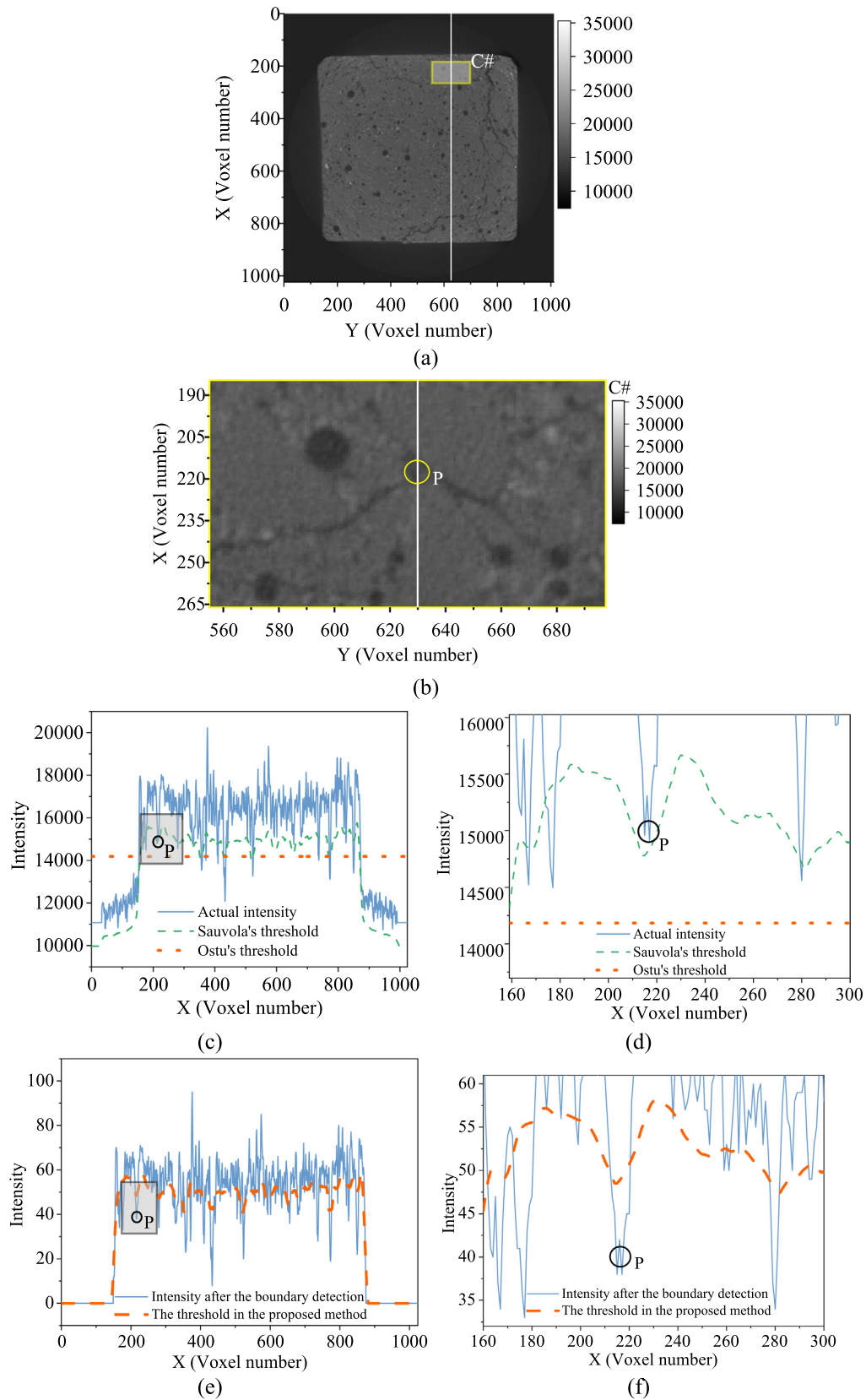


**Fig. 9.** Recognition results of three segmentation methods for the objects on the line Y = 630 (voxel number) in the specimen: (a) the line Y = 630 (voxel number) in the 25th image in the loading orientation of the specimen with a 5% rubber content, where the small cracks in area C# marked with a white rectangle; (b) area C# in (a); (c) the results of Otsu's and Sauvola's methods on the line Y = 630 (voxel number); (d) the local image around point P in (c); (e) the result in the proposed method; and (f) the local image around point P in (e).

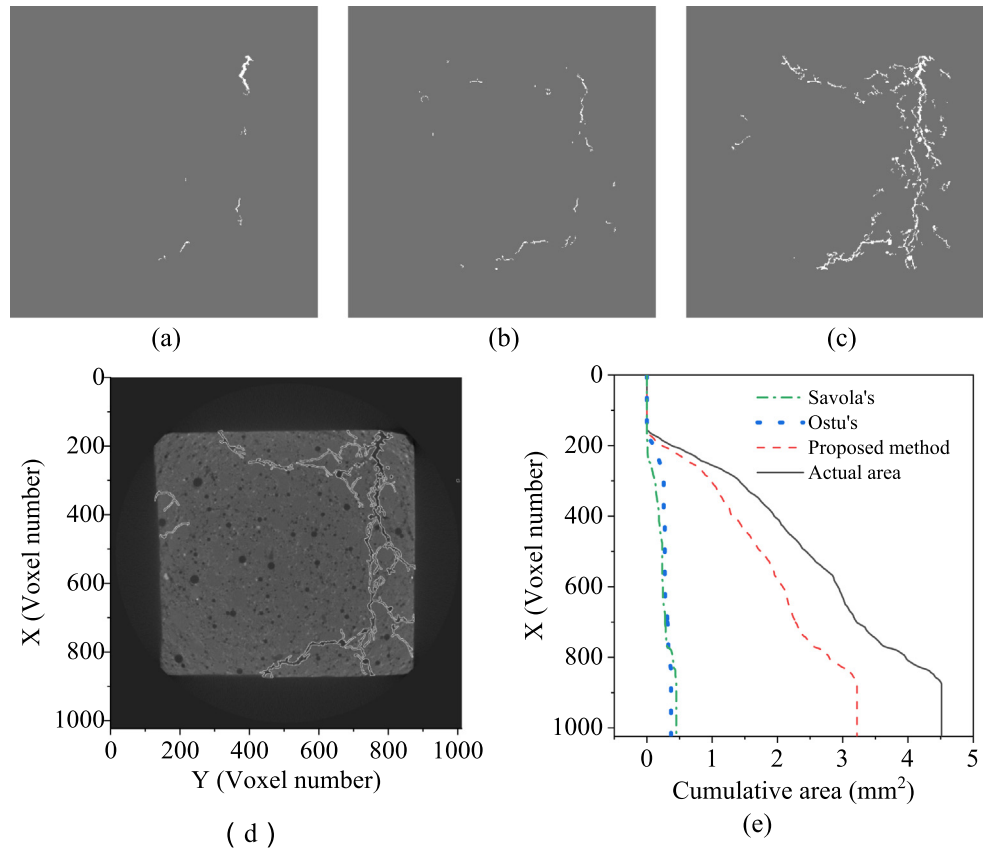


**Fig. 10.** Cracks detection results: (a) Otsu's method; (b) Sauvola's method; (c) proposed method; (d) manually marked cracks; and (e) accuracy of detected cracks.

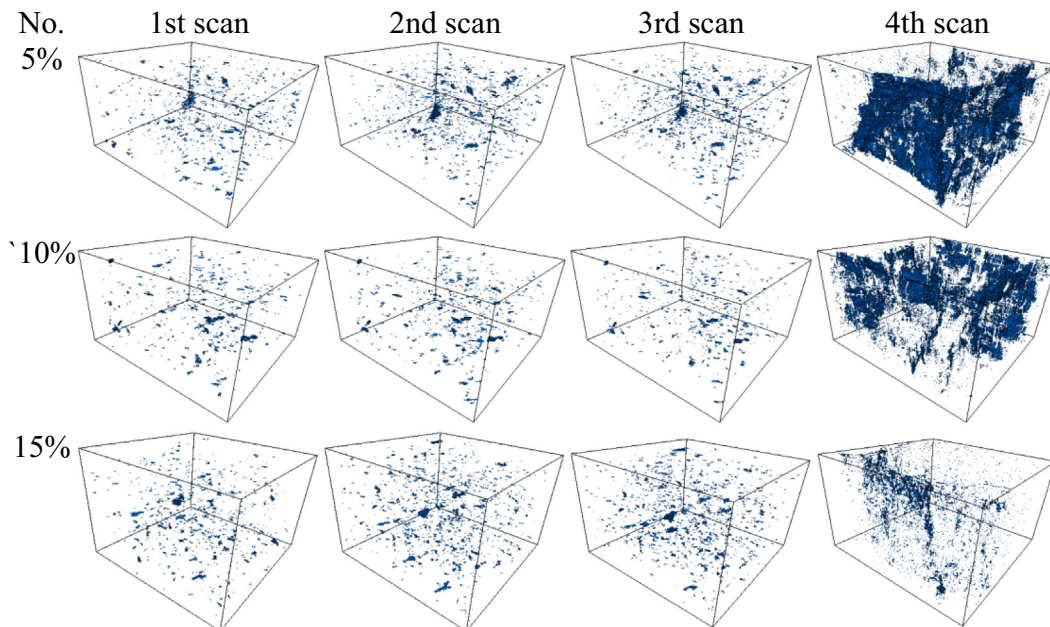


**Fig. 11.** Cracking propagation in the specimens with different rubber contents when loading.

son that because the background detection in the proposed method improved the contrast in the image, enabling the cracks easier to be detected. This result further demonstrated that the proposed method was more precise when detecting cracks than the other methods.

### 7.3. Fracture characteristics of specimens with different rubber contents

It was proven that this method is more accurate than the traditional methods and can detect microcracks. After using the

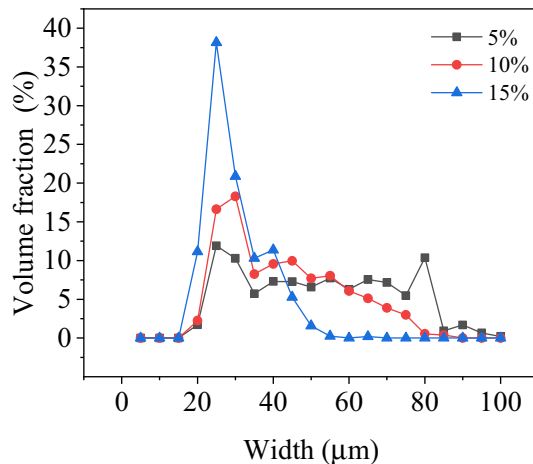


Fig. 12. Distribution of the cracks with different widths.

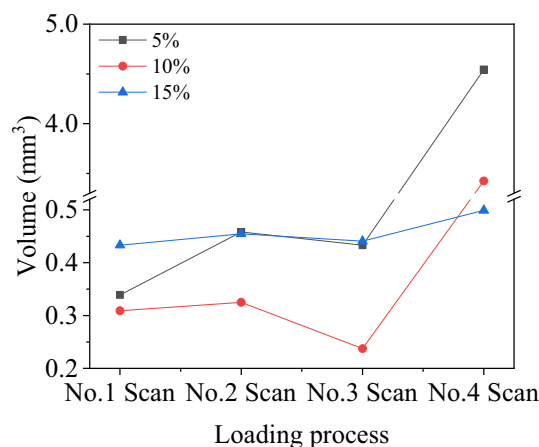


Fig. 13. Volume of the cracks when loading.

method, the 3D images of the cracks under loading could be obtained, as shown in Fig. 11.

The XCT images of the specimens with different rubber contents when loaded were processed, and 3D images of the cracks were obtained, as shown in Fig. 11. To further study the development of the cracks in rubberized concrete under loading, the equivalent width and volume of each 26-connected component [42] in the 3D volumetric images, which was taken as an independent crack, were measured, and their statistical characteristics were analyzed. In Fig. 12, the volumes and widths of the cracks were studied, and the cumulative volume fraction was computed per 5  $\mu\text{m}$  of the width. For a crack, the diameter of a cylinder of equal volume and equal surface area was defined as the width.

As shown in Fig. 12, the fraction of the small cracks with widths lower than 40  $\mu\text{m}$  increased gradually when ultimately loaded with the change in the rubber content from 5% to 15%. However, the fractions of large cracks with widths higher than 60  $\mu\text{m}$  decreased gradually. Thus, a higher rubber content introduced more small cracks and fewer large cracks. This can be explained by a decrease in the brittleness but an increase in the ductility with the addition of rubber particles [6]. The above cracking patterns in rubberized concrete agree with previous studies [21,43] when subjected to uniaxial compression.

To determine how the cracks changed during loading, the total volume of the cracks in each scan was computed. As shown in

Fig. 13, the volume of the cracks was smaller with a higher rubber content when ultimately loaded due to the strength being too low. Besides, the cracks in all the specimens had the same characteristics when loading, i.e., the total volume increased first, then decreased, and finally increased sharply during ultimate loading. During the loading process, the compressive stress was initially withstood by the concrete components of the specimens, resulting in an increase in the number of cracks due to the brittleness as the load increased from 0% to 50% of the ultimate load. When the load continued to increase, the rubber particles with high elastic moduli began to withstand the residual stress. Consequently, the volume of the cracks decreased until the 90% ultimate load. With the load changing from 90% to the ultimate load, the concrete part bore the residual component of the stress again after the rubber particles reached a limit, causing a sharp change of the volume, as shown in Fig. 13. The results further showed that the addition of the rubber improved the ductility and the resistance to cracking.

## 8. Conclusion

The cracking propagation of rubberized concrete with different rubber contents was investigated by using XCT under in-situ loading and was visualized using the proposed method. Also, the advantages and accuracy of the proposed method over the traditional method were quantified. The following conclusions were obtained:

- 1) The proposed method could distinguish the regions of the specimen and the outside air. Furthermore, the incorrect classification of cracks connected to the outside as air was avoided.
- 2) The threshold method used in the proposed method was more accurate than the traditional methods in detecting cracks, and microcracks in the images were better recognized.
- 3) In this method, the raw data were processed in three orthogonal directions, and the cracks were extracted accurately by separation, where the pores connected to the cracks could be removed, and the errors were reduced effectively.
- 4) The fracture process in the concrete with different rubber contents under loading could be visualized and compared quantitatively. From the experimental results, it could be found that the addition of rubber reduced the brittleness of the concrete, resulting in smaller cracks, while fewer large cracks appeared in the specimens when ultimately loaded. Moreover, the changes in the total volume of the cracks under loading further suggest that the rubber improved the ductility and the resistance to cracking.

## CRediT authorship contribution statement

**Shuxian Hong:** Data curation, Resources, Validation, Visualization. **Chuan Kuang:** Formal analysis, Writing - original draft, Writing - review & editing. **Jianchao Zhang:** Investigation, Software. **Dongshuai Hou:** Resources, Validation. **Jinrui Zhang:** Resources, Validation. **Laibao Liu:** Methodology, Conceptualization. **Biqin Dong:** Conceptualization, Project administration, Funding acquisition, Supervision.

## Declaration of Competing Interest

The authors declare that they have no known competing financial interests or personal relationships that could have appeared to influence the work reported in this paper.

## Acknowledgments

The authors would like to acknowledge the financial support provided by the National Natural Science Foundation of China, China (No. U1801254/51925805/51727813), Project of Department of Education of Guangdong Province, China (No. 2018KZDXM060).

## References

- [1] R. Diaz, G. Colomines, E. Peuvrel-Disdier, R. Deterre, Thermo-mechanical recycling of rubber: Relationship between material properties and specific mechanical energy, *J. Mater. Process. Technol.* 252 (2018) 454–468.
- [2] P. Sukontasukkul, C. Chaikaew, Properties of concrete pedestrian block mixed with crumb rubber, *Constr. Build. Mater.* 20 (7) (2006) 450–457.
- [3] A.M. Rashad, A comprehensive overview about recycling rubber as fine aggregate replacement in traditional cementitious materials, *Int. J. Sustainab. Built Environ.* 5 (1) (2016) 46–82.
- [4] A. Turatsinze, S. Bonnet, J.L. Granju, Potential of rubber aggregates to modify properties of cement based-mortars: improvement in cracking shrinkage resistance, *Constr. Build. Mater.* 21 (1) (2007) 176–181.
- [5] R. Si, J. Wang, S. Guo, Q. Dai, S. Han, Evaluation of laboratory performance of self-consolidating concrete with recycled tire rubber, *J. Cleaner Prod.* 180 (2018) 823–831.
- [6] A.C. Ho, A. Turatsinze, R. Hameed, D.C. Vu, Effects of rubber aggregates from grinded used tyres on the concrete resistance to cracking, *J. Cleaner Prod.* 23 (1) (2012) 209–215.
- [7] I.B. Topçu, The properties of rubberized concretes, *Cem. Conc. Res.* 25 (2) (1995) 304–310.
- [8] L.-J. Li, G.-R. Tu, C. Lan, F. Liu, Mechanical characterization of waste-rubber-modified recycled-aggregate concrete, *J. Cleaner Prod.* 124 (2016) 325–338.
- [9] B.S. Thomas, R.C. Gupta, Long term behaviour of cement concrete containing discarded tire rubber, *J. Cleaner Prod.* 102 (2015) 78–87.
- [10] I. Marie, Zones of weakness of rubberized concrete behavior using the upv, *J. Cleaner Prod.* 116 (2016) 217–222.
- [11] O. Youssfi, R. Hassanli, J.E. Mills, M. Abd Elrahman, An experimental investigation of the mechanical performance and structural application of leca-rubcrete, *Constr. Build. Mater.* 175 (2018) 239–253.
- [12] W.H. Yung, L.C. Yung, L.H. Hua, A study of the durability properties of waste tire rubber applied to self-compacting concrete, *Constr. Build. Mater.* 41 (2013) 665–672.
- [13] L. Zheng, X. Sharon Huo, Y. Yuan, Experimental investigation on dynamic properties of rubberized concrete, *Constr. Build. Mater.* 22 (5) (2008) 939–947.
- [14] M. Gesoglu, E. Güneyisi, O. Hansu, S. İpek, D.S. Asaad, Influence of waste rubber utilization on the fracture and steel-concrete bond strength properties of concrete, *Constr. Build. Mater.* 101 (2015) 1113–1121.
- [15] A.-T. Akono, J. Chen, S. Kaewunruen, Friction and fracture characteristics of engineered crumb-rubber concrete at microscopic lengthscale, *Constr. Build. Mater.* 175 (2018) 735–745.
- [16] S.Y. Alam, A. Loukili, Effect of micro-macro crack interaction on softening behaviour of concrete fracture, *Int. J. Solids Struct.* 182–183 (2020) 34–45.
- [17] B.S. Thomas, R.C. Gupta, A comprehensive review on the applications of waste tire rubber in cement concrete, *Renew. Sustain. Energy Rev.* 54 (2016) 1323–1333.
- [18] S.X. Hong, P. Liu, J.C. Zhang, F. Xing, B.Q. Dong, Visual & quantitative identification of cracking in mortar subjected to loads it using x-ray computed tomography method, *Cement Concrete Comp* 100 (2019) 15–24.
- [19] Z. Yang, W. Ren, R. Sharma, S. McDonald, M. Mostafavi, Y. Vertyagina, T.J. Marrow, In-situ x-ray computed tomography characterisation of 3d fracture evolution and image-based numerical homogenisation of concrete, *Cem. Concr. Comp.* 75 (2017) 74–83.
- [20] B. Dong, G. Fang, Y. Liu, P. Dong, J. Zhang, F. Xing, S. Hong, Monitoring reinforcement corrosion and corrosion-induced cracking by X-ray microcomputed tomography method, *Cem. Concr. Res.* 100 (2017) 311–321.
- [21] Q. Han, G. Yang, J. Xu, Z. Fu, G. Lacidogna, A. Carpinteri, Acoustic emission data analyses based on crumb rubber concrete beam bending tests, *Eng. Fract. Mech.* 210 (2019) 189–202.
- [22] K. Bisht, P.V. Ramana, Evaluation of mechanical and durability properties of crumb rubber concrete, *Constr. Build. Mater.* 155 (2017) 811–817.
- [23] D.D. Maki, B.A. Birnbaum, D.P. Chakraborty, J.E. Jacobs, B.M. Carvalho, G.T. Herman, Renal cyst pseudoenhancement: beam-hardening effects on ct numbers, *Radiology* 213 (2) (1999) 468–472.
- [24] F.E. Boas, D. Fleischmann, Ct artifacts: causes and reduction techniques, *Imag. Med.* 4 (2) (2012) 229–240.
- [25] N. Otsu, A threshold selection method from gray-level histograms, *IEEE Trans. Syst., Man, Cybern.* 9 (1) (1979) 62–66.
- [26] Z.J. Yang, B.B. Li, J.Y. Wu, X-ray computed tomography images based phase-field modeling of mesoscopic failure in concrete, *Eng. Fract. Mech.* 208 (2019) 151–170.
- [27] E.N. Landis, E.N. Nagy, Three-dimensional work of fracture for mortar in compression, *Eng. Fract. Mech.* 65 (2) (2000) 223–234.
- [28] P.A. Cheremkhin, E.A. Kurbatova, Comparative appraisal of global and local thresholding methods for binarisation of off-axis digital holograms, *Opt. Lasers Eng.* 115 (2019) 119–130.
- [29] Y. Huang, D. Yan, Z. Yang, G. Liu, 2d and 3d homogenization and fracture analysis of concrete based on in-situ x-ray computed tomography images and monte carlo simulations, *Eng. Fract. Mech.* 163 (2016) 37–54.
- [30] Ł. Skarżyński, J. Tejchman, Experimental investigations of damage evolution in concrete during bending by continuous micro-ct scanning, *Mater. Charact.* 154 (2019) 40–52.
- [31] C. Lu, J. Yu, C.K.Y. Leung, An improved image processing method for assessing multiple cracking development in strain hardening cementitious composites (shcc), *Cem. Concr. Compos.* 74 (2016) 191–200.
- [32] J. Sauvola, T. Seppanen, S. Haapakoski, M. Pietikainen, Adaptive document binarization, *Proceedings of the Fourth International Conference on Document Analysis and Recognition*, 1997, pp. 147–152 vol. 1.
- [33] J. Sauvola, M. Pietikainen, Adaptive document image binarization, *Pattern Recogn.* 33 (2) (2000) 225–236.
- [34] Y. Tan, K. Kiekens, J.-P. Kruth, A. Voet, W. Dewulf, Material dependent thresholding for dimensional x-ray computed tomography, *2011 International symposium on digital industrial radiology and computed tomography: June 20–22, 2011, Berlin, Germany, Berlin(DE), 2011*, pp. 83–90.
- [35] Q. Dong, B. Huang, X. Shu, Rubber modified concrete improved by chemically active coating and silane coupling agent, *Constr. Build. Mater.* 48 (2013) 116–123.
- [36] F. Abbassi, F. Ahmad, Behavior analysis of concrete with recycled tire rubber as aggregate using 3d-digital image correlation, *J. Cleaner Prod.* (2020), 123074.
- [37] G.T. 17671–1999, Method of testing cements–determination of strength [s], State Bureau of Quality and Technical Supervision of China, 1999.
- [38] K. Wu, E. Otoo, K. Suzuki, Optimizing two-pass connected-component labeling algorithms, *Pattern Anal. Appl.* 12 (2) (2008) 117–135.
- [39] S. Dražić, N. Sladoje, J. Lindblad, Estimation of feret's diameter from pixel coverage representation of a shape, *Pattern Recogn. Lett.* 80 (2016) 37–45.
- [40] S.C. Satapathy, N.S.M. Raja, V. Rajinikanth, A.S. Ashour, N. Dey, Multi-level image thresholding using otsu and chaotic bat algorithm, *Neural Comput. Appl.* 29 (12) (2018) 1285–1307.
- [41] H. Kim, E. Ahn, S. Cho, M. Shin, S.-H. Sim, Comparative analysis of image binarization methods for crack identification in concrete structures, *Cem. Concr. Res.* 99 (2017) 53–61.
- [42] L. Perrotton, Contour tracking of 3d 26-connected discrete objects, *SPIE1994*.
- [43] J. Xu, Z. Fu, Q. Han, G. Lacidogna, A. Carpinteri, Micro-cracking monitoring and fracture evaluation for crumb rubber concrete based on acoustic emission techniques, *Struct. Health Monit.* 17 (4) (2017) 946–958.